

# Deep Planar Parallax for Monocular Depth Estimation

Haoqian Liang<sup>1</sup> Zhichao Li<sup>2</sup> Ya Yang<sup>1\*</sup> Naiyan Wang<sup>2</sup>

<sup>1</sup>Beijing University of Posts and Telecommunications <sup>2</sup>TuSimple

{lianghq, yangya}@bupt.edu.cn, {leeisabug, winsty}@gmail.com

## Abstract

*Depth estimation is a fundamental problem in the perception system of autonomous driving scenes. Although autonomous driving is challenging, much prior knowledge can still be utilized, by which the sophistication of the problem can be effectively restricted. Some previous works introduce the road plane prior to the depth estimation problem according to the Planar Parallax Geometry. However, we find that their usages are not effective, leaving the network cannot learn the geometric information. To this end, we analyze this problem in detail and reveal that explicit warping of consecutive frames and flow pre-training can effectively bring the geometric prior into learning. Furthermore, we propose Planar Position Embedding to deal with the intrinsic weakness of plane parallax geometry. Comprehensive experimental results on autonomous driving datasets like KITTI and Waymo Open Dataset (WOD) demonstrate that our Planar Parallax Network(PPNet) dramatically outperforms existing learning-based methods.*

## 1. Introduction

Depth perception is at the core of 3D computer vision task. Benefiting the data-driven approach, recent work has shown that learning-based methods [1, 4, 5, 9, 21, 24, 31, 55] can estimate the geometric properties such as depth or pose in one single forward pass. However, pure deep learning based methods usually suffer from serious generalization problems [25, 50, 57, 65], and not as robust as traditional theoretically sound approaches. Consequently, recent methods introduce geometric constraints or priors into deep learning approaches to regularize the solution space. For example, [61, 63] utilize epipolar geometry for better generalization and scale consistency in depth estimation. [26, 30] incorporate Singular Value Decomposition (SVD) into deep point cloud registration to get the final pose.

For the depth estimation problem in the autonomous driving system, the following crucial assumptions exist: the



Figure 1. The first row shows current frame superimposed by the homography warping of previous frame based on planar parallax geometry, in which if the pixel is higher than the plane, the shearing is heavier. The second row shows the flow estimated by a pre-trained optical flow model between the two images in first row. Furthermore, the last row displays our depth estimation results based on the estimated flow.

objects and obstacles are all placed on a known road plane, and we could access multiple consecutive frames and know ego-motion between the frames. This assumption naturally leads to the planar parallax (P+P) geometry [40, 43]. In particular, The P+P geometry shows that the 3D scene structure after the alignment of consecutive frames to the reference plane can be derived from the residual pixel displacements caused by the camera's motion. As the formulation is shown in Sec. 3, P+P methods save the capacity for estimating the depth of ground and eliminate the dependencies in estimating camera *rotation*. Consequently, [53, 59] follows the P+P framework, using a neural network to predict pixel-wise  $\gamma$ , which is the ratio of height to depth rather than a depth map. Nevertheless, we argue that they are reasonable attempts, but it does not enjoy the gains of geometric

\*Corresponding author.

priors. It is unachievable to guide the model to learn geometric information only depending on the supervision of  $\gamma$ . We perform detailed experiments to investigate whether the P+P pipeline benefits the depth estimation network.

In this paper, we are committed to fully utilising the P+P geometric priors. Intuitively, additional parallax supervision can force the network to learn the residual displacement, which can derive the  $\gamma$ . However, parallax ground truth in real-world data is costly, so we choose a more easy but practical way. We reveal that a well pre-trained optical flow network can keep the ability to estimate the residual pixel displacements, dramatically improving depth estimation results. Regarding the challenge of moving objects, because it violates the rigid motion assumption of P+P, we follow DfM [51] to involve a single view path with learnable weights to compensate. Moreover, as derived about  $\gamma$  and depth, the depth estimation will be very sensitive to pixel error for pixels higher than the camera or near the epipole. To remedy this issue, we propose Planar Position Embedding (PPE), which makes the network aware of the relative position to the reference plane of each pixel, guiding the network to choose whether to depend more on geometry or statistics.

To summarize, our main contributions are three-folds:

- We propose a deep planar parallax depth estimation network, which effectively incorporates planar parallax geometry pipeline and data-driven methods. For the first time, we demonstrate that optical flow pre-training is crucial for using geometric prior.
- We also propose a Planar Position Embedding which introduces the pixel position related to the reference plane into the network. It overcomes the inherent defect of the learning based planar parallax framework.
- We test our proposed method on large-scale self-driving datasets, KITTI [13] and Waymo Open Dataset (WOD) [46]. Extensive results demonstrate that our method beats the state-of-the-art methods by a large margin about 28.8%.

## 2. Related Work

## 2.1. Monocular Depth Estimation

Eigen *et al.* [11] are the ones who first utilize CNN for the monocular depth estimation task. They predict depth from a single image by combining local and global information. Since then, methods based on neural networks have gained significant improvement [12, 22, 56]. In recent years, Vision transformers have been introduced to depth estimation tasks. Adabin [3] uses a transformer-based architecture to divide the depth range into bins. NeWCRFs [60] adopt Swin Transformer [27] as encoder and a fully-connected

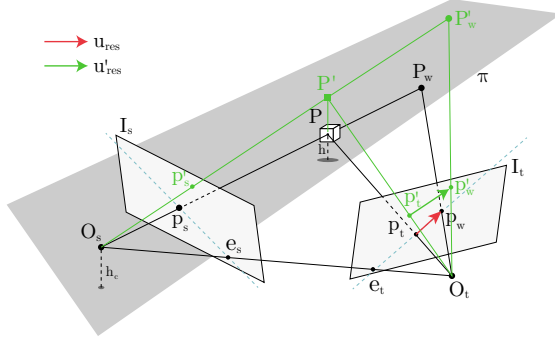


Figure 2. The illustration of planar parallax geometry.

Conditional Random Field(CRF) as decoder, which made a considerable improvement. Despite learning from a single image, some other work focus on using monocular videos. Monocular videos are mainly used by self-supervised models [14, 19, 23, 32, 39, 44, 49, 57, 66, 67]. Geometric constraints are built between consecutive frames to reduce the dependency on ground-truth depth. We believe that geometric information can not only provide supervision in unsupervised settings but also help supervised methods to achieve better performance and generalization.

## 2.2. Flow Estimation

Start from FlowNet series [10, 15], end-to-end optical flow networks have shown their superiority in flow estimation tasks. After that, PWC-Net [45] introduces the pyramid(P), warping(W), and cost volume(C) into network design and significantly improves the performance. Mask-FlowNet [62] resolves the occluded areas during warping by a self-learned occlusion mask. The success of RAFT [47] lies in the iterative refinement on the cost volumes. GM-Flow [54] first uses a transformer in flow estimation. Along with the supervised methods, photometric loss based unsupervised flow [18, 35, 52, 64] achieves researchers' attention, but there still exists a gap in performance compared with supervised methods. Optical flow is a fundamental low-level task that plays an essential role in many downstream problems. We use it as a geometric prior so that the network can more efficiently use the geometric information to estimate the depth.

## 2.3. Planar Parallax Methods

The planar parallax methods were first proposed in the mid-90s in [40, 41, 43]. After choosing a reference plane, this method decomposes the motion between multiple frames into planar homography and residual pixel displacement from the unaligned pixels [16]. The planar homography can be computed by camera  $z$  axis translation and plane normal vector. The residual pixel displacements can

be obtained by feature matching methods such as optical flow. In this way, P+P geometry significantly reduces the estimation space. Many applications [8, 17, 42, 58] depends on a plane in the scene. For example, in robotics [2, 29], the height of points from the ground plane is crucial. Moreover, Jung *et al.* [20] propose a method based on planar parallax for quantifying image stitching, and Vaish *et al.* [48] use it in camera calibration. A critical problem in these methods is finding a suitable reference plane. Naturally, in driving scenes, the road plane can easily be extracted from LiDAR points or high-precision maps. Taking these advantages, Yuan *et al.* [59] proposed a new solution combining traditional planar parallax geometry with a deep neural network for road environment. Xing *et al.* [53] uses the dense structure information provided by P+P as depth hints. During our experiments, we found that previous learning-based P+P methods do not fully utilize the geometry structure. In this paper, we will pursue this goal.

### 3. Method

In this section, we first briefly review planar parallax geometry, showing how the method connects 3D structure  $\gamma$  with residual image displacement. And then, we elaborate on combining this method with deep learning, which enjoys the best of two worlds.

#### 3.1. Planar Parallax Geometry

For better understanding, we use capital letter to represent 3D points, lowercase letter for 2D points, bold font for vectors, and matrix in calligraphy. As [16] shown, the ratio of height to depth  $\gamma$  plays an important role in modeling the homography as a 2D projective transformation. In particular,

$$\gamma = \frac{h}{z}, \quad (1)$$

where  $h$  and  $z$  is the height and depth of a pixel.

In Fig. 2, we describe the geometry visually. Define  $\mathbf{P}_s = (x', y', z')^T$  and  $\mathbf{P}_t = (x, y, z)^T$  as the coordinates of a point  $\mathbf{P}$  in source view and target view, separately. Let  $\mathcal{R}$  and  $\mathbf{T} = (t_x, t_y, t_z)^T$  denote the rotation matrix and translation vector between the two camera views. The transformation from  $\mathbf{P}_s$  to  $\mathbf{P}_t$  can be written as:

$$\mathbf{P}_t = \mathcal{R}\mathbf{P}_s + \mathbf{T}. \quad (2)$$

The height above the reference plane  $\pi$  of the point  $\mathbf{P}_t$  can be express as:

$$h = h_c - \vec{\mathbf{N}}^T \mathbf{P}_t, \quad (3)$$

where  $\vec{\mathbf{N}}^T$  is the normal of plane  $\pi$  and  $h_c$  is the height of the camera.

Let  $\mathbf{p}_s = \frac{1}{z} \mathcal{K} \mathbf{P}_s$ ,  $\mathbf{p}_t = \frac{1}{z} \mathcal{K} \mathbf{P}_t$  and  $\mathbf{t} = \mathcal{K} \mathbf{T}$ , where  $\mathcal{K}$  is intrinsic matrix of the camera. The homography matrix between the two images can be written as:

$$\mathcal{H} = \mathcal{K}(\mathcal{R} + \frac{\mathbf{T} \vec{\mathbf{N}}^T}{h_c}) \mathcal{K}^{-1}. \quad (4)$$

Define  $\mathbf{p}_w$  as the  $\mathbf{p}_s$  warped by homography  $\mathcal{H}$ ,

$$\mathbf{p}_w = \mathcal{H} \mathbf{p}_s \quad (5)$$

As shown in Fig. 2,  $\mathbf{u}_{res} = \mathbf{p}_w - \mathbf{p}_t$  is the residual flow. Following the mathematical derivation in [16, 59], when  $t_z \neq 0$ , we can obtain:

$$\mathbf{u}_{res} = \frac{\gamma \frac{t_z}{h_c}}{1 - \gamma \frac{t_z}{h_c}} (\mathbf{p}_t - \mathbf{e}_t), \quad (6)$$

where  $\mathbf{e}_t = \frac{1}{t_z} \mathbf{t}$  is the epipole in the target view, which denotes the point that does not move after the warping. For detailed derivation, we refer the readers to the appendix. In Fig. 2,  $\mathbf{P}'$  is a 3D point higher than  $\mathbf{P}$ . Because  $\gamma = h/z$ , for the points with the same depth  $z$ , the higher it is, the residual flow is larger, equivalently  $\mathbf{u}_{res} > \mathbf{u}_{res}'$ . The first row in Fig. 1 also shows that intuitively. The higher position has larger distortion. This is the key geometric clue for 3D structure.

From Eqn. 6, we can conclude that the residual flow always moves towards or away from the epipole, and has a strong relationship with  $\gamma$ . We can also convert Eqn. 6 to

$$\gamma = \frac{h_c}{t_z(1 + \frac{\mathbf{p}_t - \mathbf{e}_t}{\mathbf{u}_{res}})}. \quad (7)$$

Except the relationship with residual flow,  $\gamma$  can also perform 3D reconstruction. Since  $\mathbf{P}$  can be calculated by an inverse projection

$$\mathbf{P}_t = z \mathcal{K}^{-1} \mathbf{p}_t. \quad (8)$$

By substituting it into Eqn. 3, we can obtain an important formula discussed in proposed Planar Position Embedding.

$$\vec{\mathbf{N}}^T (\mathcal{K}^{-1} \mathbf{p}_t) = \frac{h_c - h}{z}. \quad (9)$$

Eqn. 9 can be finally transformed into

$$z = \frac{h_c}{\gamma + \vec{\mathbf{N}}^T (\mathcal{K}^{-1} \mathbf{p}_t)}. \quad (10)$$

We could use it to convert predicted  $\gamma$  to depth results given the plane and camera height above the plane. Compared with epipolar geometry, the superiority of the P+P geometry is twofold: First, as shown in the first row in Fig. 1, the road pixel in the image is aligned without disparity after warping by road homography. It saves the network capacity for estimating the depth of the ground. Second, Eqn. 7 is only affected by  $t_z$ , which removes the dependency on the rotation, reducing the error caused by ego-motion noise.

⊕ Weighted Sum  
 ⊖ Embedding Layer

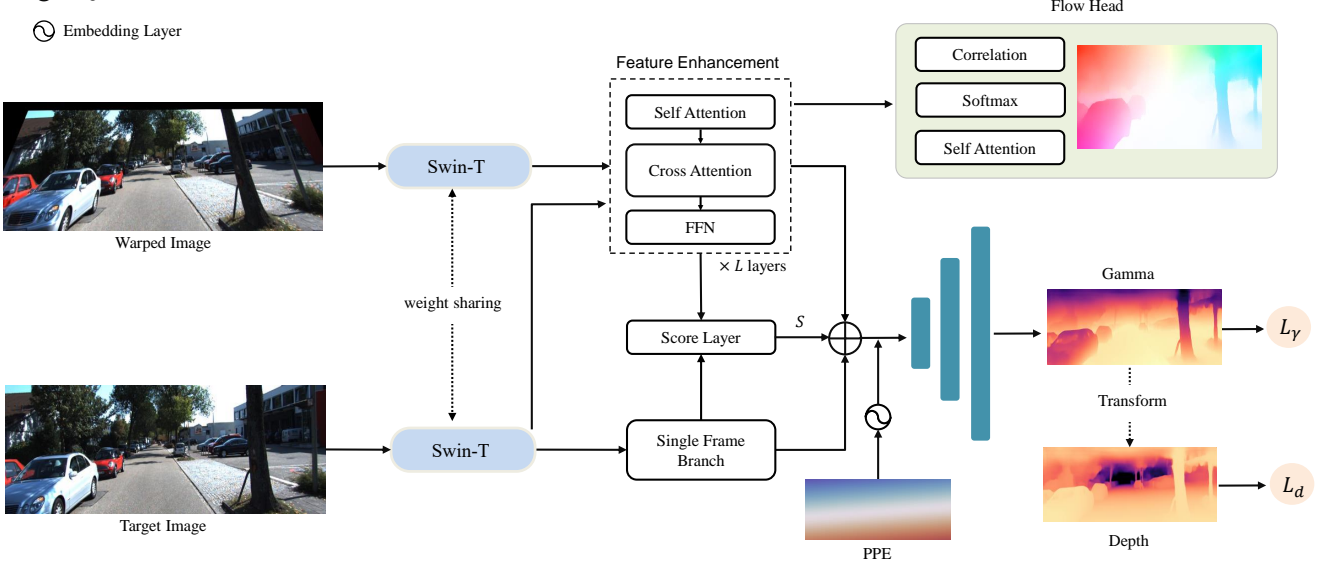


Figure 3. Overview of the proposed Planar Parallax Network. Given two plane-aligned images, we first extract features by a swin-tiny backbone. And then we divide two streams, a flow branch and a single frame branch. In flow branch, we follow the Feature Enhancement module and Flow Head in GMflow [54]. The Flow Head is only used in flow pretrain. The Single Frame Branch is a simple conv net and fused with flow branch by weighted sum. The network is supervised by gamma loss  $L_\gamma$  and depth loss  $L_d$ .

### 3.2. Planar Parallax Network

**Flow Network Pre-training** As shown in Eqn. 7, given the height of the camera and the translation along the forward axis,  $\gamma$  can be described by residual flow based on plane-aligned images. The pixel fall on the plane has zero height which leads to  $\gamma = 0, \mathbf{u}_{res} = 0$ , and the flow can reconstruct the height and depth. To enhance the accuracy of residual flow, we try to introduce geometric prior by pre-training the network by flow estimation task [54, 62]. After that, the  $\gamma$  prediction becomes a much easier assignment. As in Tab. 3, the flow pre-training brings significant improvement.

**Prediction for Dynamic Objects** For moving objects that violate the underlying static scene assumption in Sec. 3.1, we follow the recent work DfM [51] that introduces an additional component. It utilizes only the reference image as input and predicts  $\gamma$ , which mainly benefits from the training data and network’s generalization power. This branch is fused into the primary branch as:

$$\mathcal{S} = \sigma[\phi(\mathcal{F}_m, \mathcal{F}_s)], \quad (11)$$

$$\mathcal{F} = \mathcal{S} \circ \mathcal{F}_m + (1 - \mathcal{S}) \circ \mathcal{F}_s, \quad (12)$$

where  $\sigma$  is the sigmoid function.  $\circ$  is element-wise multiplication.  $\phi$  is a simple convolutional layer, which outputs fusion score  $\mathcal{S}$  guiding the fusion of the single-frame feature  $\mathcal{F}_s$  and multi-frame feature  $\mathcal{F}_m$ .

**Planar Position Embedding (PPE)** In P+P methods, there are two parameters the camera’s intrinsic  $\mathcal{K}$  and normal vector of the plane  $\vec{\mathbf{N}}^T$ . The network should be aware these two variables. Inspired by position embedding from transformer models, we propose Planar Position Embedding, which combines these two into one formula  $\vec{\mathbf{N}}^T(\mathcal{K}^{-1}\mathbf{p})$ . As shown in Eqn. 9, the PPE is the projection of the point in the normalized image plane on the normal direction of the reference plane. We show the visualization of PPE in Fig. 3. PPE distinctly describes the trend of change when the plane is tilted in the camera. We use it as the pixel’s position related to the reference plane and build embedding as follows:

$$\mathcal{F} = \phi(\mathcal{E}) \quad (13)$$

$$\mathcal{E}_{ij} = \vec{\mathbf{N}}^T(\mathcal{K}^{-1}\mathbf{p}_{ij}) \quad (14)$$

where  $\phi$  is a simple convolutional network. It lets the network aware the relative position of the plane, suppressing some absurd errors. We investigate its effectiveness in Sec. 4.4.

**Overall Structure** Combining the method mentioned above, we propose a new framework named PPNet. As shown in Fig. 3, the network takes two consecutive images  $I_{t-1}$  and  $I_t$  as input. image  $I_{t-1}$  is warped using road plane homography. The network outputs  $\gamma$  map of image  $I_t$ , which is then transformed into depth map using Eqn. 10. We adopt the feature extraction and feature enhancement component introduced in GMFlow [54] and leave the feature matching and flow propagation only for flow pre-training.

We replace the CNN backbone in GMFlow with a Swin Transformer [27] for greater model capacity. The  $\frac{1}{8}$  downsampled feature map is fed into feature enhancement transformer, where the P+P geometry can be analyzed. The  $\frac{1}{32}$  downsampled feature map is used for single frame estimation, which is then fused with the output of the feature enhancement transformer. After the fusion, planar position embedding will be introduced. The final feature is upsampled to the original size to output  $\gamma$ .

**Training Loss.** Following previous work [3, 11, 22, 59, 60], we use a L1 loss to supervise  $\gamma$  and a Scale-Invariant Logarithmic (SILog) loss to supervise the depth obtained by  $\gamma$  using Eqn. 10. If the total number of pixels with ground-truth is  $N$ , the loss for  $\gamma$  can be defined as

$$L_\gamma = \frac{1}{N} \sum_i |\gamma_i - \gamma_i^*|, \quad (15)$$

where  $\gamma_i$  and  $\gamma_i^*$  are the predicted  $\gamma$  value and corresponding ground-truth.

The logarithm difference is defined as

$$\Delta d_i = \log d_i - \log d_i^*, \quad (16)$$

where  $d_i$  and  $d_i^*$  are the predicted depth value obtained by  $\gamma$  using Eqn. 10 and its corresponding ground-truth depth value. Then the depth loss is defined as:

$$L_d = \alpha \sqrt{\frac{1}{N} \sum_i \Delta d_i^2 - \frac{\lambda}{N^2} (\sum_i \Delta d_i)^2}, \quad (17)$$

where  $\lambda$  is a variance minimizing factor, and  $\alpha$  is a scale constant. Following the previous works [22, 60], we set  $\lambda = 0.85$  and  $\alpha = 10$ .

The total loss function is defined as the summation of the loss for  $\gamma$  and depth with weight  $w_\gamma$  and  $w_d$ :

$$L = w_\gamma L_\gamma + w_d L_d. \quad (18)$$

Here we set  $w_\gamma = 1$  and  $w_d = 10^{-2}$  since the depth produced by Eqn. 10 may be very unstable. Also, the network should focus more on the geometric advantage that  $\gamma$  brings.

## 4. Experiments

In this Section, we first introduce two autonomous driving datasets in Sec. 4.1, KITTI and WOD, and describe how we build the data our model needs. Then we provide the implementation details of our method in Sec. 4.2. Sec. 4.3 demonstrates that our method dramatically exceeds the previous state-of-the-art methods in both datasets. We conduct specific ablation studies in Sec. 4.4. On the one hand, we prove our main point that the flow pre-trained model effectively helps the model using the geometric prior. On the other hand, it shows that the improvements we proposed are practical and critical.

### 4.1. Datasets

We use KITTI dataset [13] and Waymo Open Dataset [46] to evaluate the performance of the proposed network.

**KITTI.** KITTI dataset is one of the most popular benchmark in Monocular Depth Estimation. We use the data split proposed by Eigen *et al.* [11], which contains 23488 training samples and 697 testing samples. We reproject all the points on the ground-truth depth map back to 3D space and extract the road plane using RANSAC algorithm. As in previous work, the homography transformation is calculated using odometry data provided by KITTI. Moreover, we fix some inaccurate pose matrix using point-to-plane ICP algorithm [7]. For the reference plane, we adopt two different settings to show the universality of our work:

- **Estimated Plane(EP).** In this setting, the road planes are extracted using the RANSAC algorithm to fit a flat plane in the scene. For the images without a road plane, we use the mean plane method below.
- **Mean Plane(MP).** In this setting, We demonstrate the capabilities of our model without the accurate planes. The mean plane is acquired by computing the mean plane normal of the estimated plane from all the frames in the dataset. Note that if we have accurate extrinsic parameters of camera w.r.t. the road plane, we could also approximately extract planes using methods like IPM [33]. However, it is not provided accurately in the dataset.

**Waymo Open Dataset.** Since the RP2-Waymo dataset [59] remains unpublished, to compare with RPANet [59], we reproduced the dataset following it. The reproduced dataset contains 12894 training samples and 1345 test samples. WOD does not have dense depth supervision. The ground-truth  $\gamma$  is built by the sparse observations from LiDAR. Although the experiments on WOD show the generalization of methods, we also argue that without a deliberate processing, the ground-truth depth from LiDAR may also lead to

Method	Backbone	Abs Rel $\downarrow$	Sq Rel $\downarrow$	RMSE $\downarrow$	RMSE log $\downarrow$	$\delta_1 \uparrow$	$\delta_2 \uparrow$	$\delta_3 \uparrow$	Params
Eigen et al. [11]	-	0.190	1.515	7.156	0.270	0.692	0.899	0.967	83 M
DORN [12]	ResNet-101	0.072	0.307	2.727	0.120	0.932	0.984	0.995	100 M
BTS [22]	ResNext-101	0.059	0.241	2.756	0.096	0.956	0.993	0.998	113 M
DPT [38]	VIT-Hybrid	0.062	0.222	2.575	0.092	0.959	0.995	0.999	123 M
Adabin [3]	EfficientNet-B5	0.058	0.190	2.360	0.088	0.964	0.995	0.999	78 M
NeW CRFs [60]	Swin-Large	0.052	0.155	2.129	0.079	0.974	0.997	0.999	270 M
Ours(MP)	Swin-Tiny	<u>0.044</u>	<u>0.127</u>	<u>1.986</u>	<u>0.069</u>	<u>0.981</u>	<u>0.997</u>	<u>0.999</u>	52 M
Ours(EP)	Swin-Tiny	<b>0.037</b>	<b>0.109</b>	<b>1.815</b>	<b>0.062</b>	<b>0.983</b>	<b>0.997</b>	<b>0.999</b>	52 M

Table 1. Quantitative results on the Eigen split of KITTI dataset. The best results are in **bold** and second best are underlined.

Method	Height	Abs Rel $\downarrow$	Sq Rel $\downarrow$	RMSE $\downarrow$	RMSE log $\downarrow$	$\delta_1 \uparrow$	$\delta_2 \uparrow$	$\delta_3 \uparrow$
RPNNet [59]	< 1m	0.036	0.198	2.707	0.080	0.974	0.992	0.997
BTS [22]	< 1m	0.044	0.166	2.383	0.075	0.980	0.995	0.998
NeW CRFs [60]	< 1m	0.043	0.155	2.321	0.072	0.981	<b>0.996</b>	<b>0.999</b>
Ours(EP)	< 1m	<b>0.029</b>	<b>0.131</b>	<b>2.200</b>	<b>0.065</b>	<b>0.984</b>	0.995	0.998
RPNNet [59]	-	0.086	1.089	5.623	0.187	0.903	0.968	0.987
BTS [22]	-	0.071	0.531	4.105	0.119	0.939	0.984	0.995
NeW CRFs [60]	-	0.067	0.459	3.866	0.112	0.945	<b>0.987</b>	<b>0.996</b>
Ours(EP)	-	<b>0.056</b>	<b>0.450</b>	<b>3.853</b>	<b>0.108</b>	<b>0.950</b>	<b>0.987</b>	0.995

Table 2. Quantitative results on the Waymo Open Dataset.



Figure 4. Mismatch examples of Waymo Open Dataset. Left Up: motion distortion. Right Up: noise of high reflectance. Left Bottom: rainy noise. Right Bottom: unknown noise.

some unexpected errors. As shown in Fig. 4, objects with high reflectance or motion distortion will mismatch the observations from the image and LiDAR.

#### 4.2. Implementation Details

We implement the proposed network using Pytorch [37]. AdamW optimizer [28] with a weight decay of  $10^{-2}$  is adopted. All experiments are preformed on Nvidia RTX 3090 GPUs. Following [22], the learning rate decrease from  $10^{-4}$  to  $10^{-5}$  using polynomial decay with power  $p = 0.9$ . Our model is trained for 20 epochs with a to-

tal batch size of 8. We use augmentation techniques such as horizontal flipping and brightness jittering. Moreover, since the P+P geometry is built on the condition  $t_z \neq 0$ , we randomly replace the warped image  $I_{t-1}$  with image  $I_t$  to improve the robustness to the static scene. Our model is first pre-trained on flow estimation task. We follow the training strategy of KITTI dataset in GMFlow [54], the model is first trained on FlyingChairs(Chairs) [10] and FlyingThings3D (Things) [34] datasets, then fine-tuned on Sintel [6] and KITTI [36] datasets.

#### 4.3. Comparisons with the state-of-the-art Depth

**Depth results on KITTI dataset** In Tab. 1, we report the results of depth estimation on KITTI, in which our model surpasses the previous state-of-the-art model by a significant margin on all the metrics. Notably, although we can easily get the estimated plane(EP) during the autonomous driving scenes, we also show the results with the mean plane(MP), which does not rely on any online estimation. With some loss of accuracy by the estimated plane, the improvement is still considerable. Fig. 5 illustrates the quantitative results. As shown in the error map, we highlight the advantages of our method in estimating obstacles. Since there are priors provided by the ground, the error of vertical and static objects are significantly improved.

**Depth results on Waymo Open Dataset** As for Waymo Open Dataset, we reproduce the RPNNet following [59]

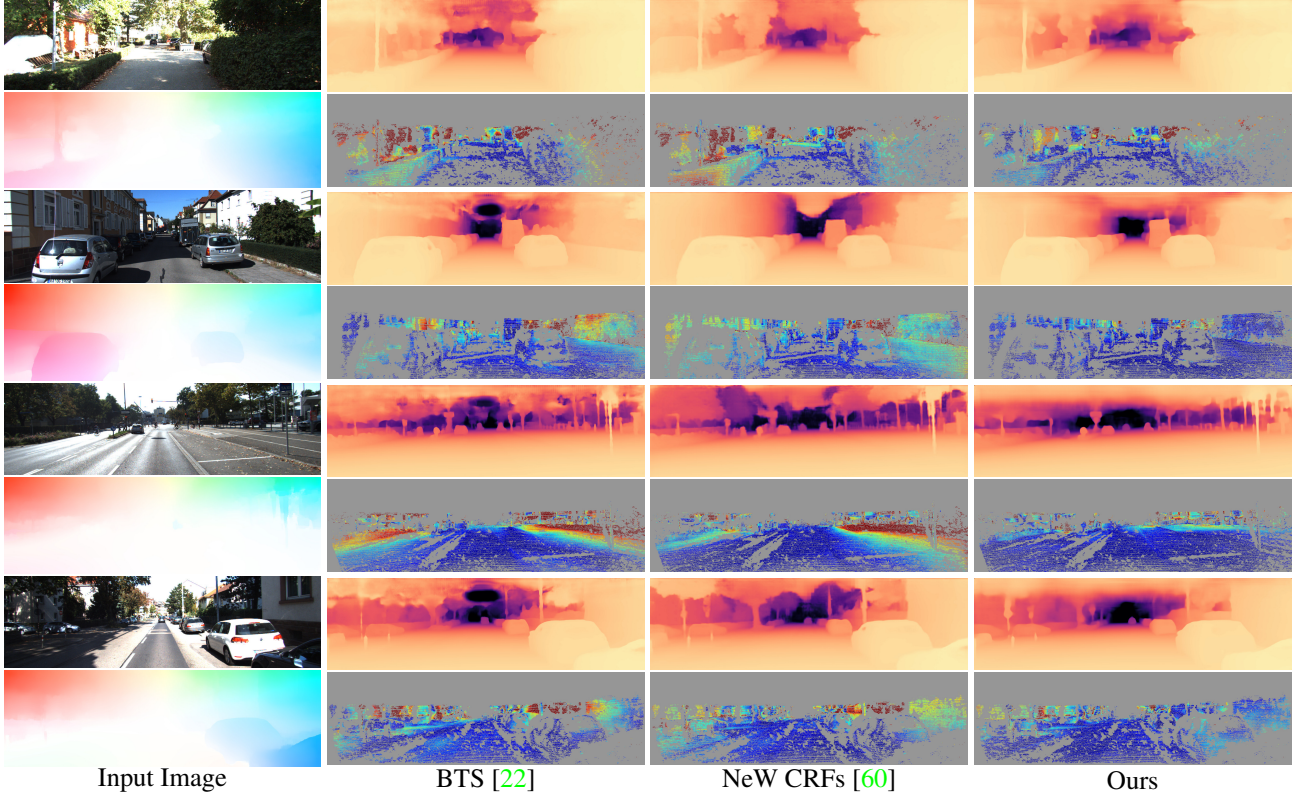


Figure 5. Qualitative results on the Eigen split of KITTI dataset. For each sample, the first column shows the target image and the flow estimated by the pre-trained optical flow model between the two plane-aligned images. The rest columns each shows the predicted depth map and the corresponding error map for a model. Blue represents smaller error, while red represents larger error.

and train BTS [22], NeW CRFs [60] with official open-sourced code for comparison<sup>1</sup>. In Tab. 2, we show the results with height  $< 1m$  and full range. Compared with the results in KITTI, PPNet still shows remarkable improvement in Abs Rel, but the improvement gap in Sq Rel has been narrowed. That means our model still has a higher accuracy, but there are more pixels with larger errors in all methods. This is because WOD includes some difficult data on nights or rainy days. Moreover, there are many slow-driving scenarios which violate the motion assumption in Eqn. 6. Despite all this, our methods show the priority in height  $< 1m$ , benefiting from the plane prior.

#### 4.4. Ablation Study

**Effectiveness of flow pre-training** To better understand the benefit flow pre-training brings, we remove the single frame branch, Planar Position Embedding, and the random data augmentation so that no extra single frame information would affect the result in this ablation study. After removing these components, we also add a condition height  $< 1m$  to highlight the influence caused by the prior of plane. In

<sup>1</sup><http://github.com/cleinc/bts>, <http://github.com/aliyun/NeWCRFs>

Target	Frame	Warp	Pretrain	Abs Rel $\downarrow$	RMSE $\downarrow$
Flow	2	N	ImageNet	0.160	5.661
Depth	1	N	ImageNet	0.059	2.059
Gamma( $\gamma$ )	1	N	-	0.055	2.271
Gamma( $\gamma$ )	2	N	-	0.054	2.231
Gamma( $\gamma$ )	2	Y	-	0.054	2.191
Gamma( $\gamma$ )	1	N	ImageNet	0.047	1.985
Gamma( $\gamma$ )	2	N	ImageNet	0.046	1.944
Gamma( $\gamma$ )	2	Y	ImageNet	0.045	1.927
Gamma( $\gamma$ )	1	N	Flow	0.044	1.965
Gamma( $\gamma$ )	2	N	Flow	0.039	1.755
Gamma( $\gamma$ )	2	Y	Flow	<b>0.035</b>	<b>1.460</b>

Table 3. Ablation studies for flow pre-training. The target flow means we use the flow prediction and compute  $\gamma$  by Eqn. 7. Frame indicates to number of consecutive frames we use. Warp denotes whether to warp with planar homography. All results are under condition height  $< 1m$ .

Tab. 3, we first show the pure geometry methods. We compute  $\gamma$  by Eqn. 7 with flow prediction from GMFlow. This method merely does not work because dynamic objects do not meet the hypothesis and some pixels near to the epipole are too sensitive to flow's precision. Furthermore, the com-

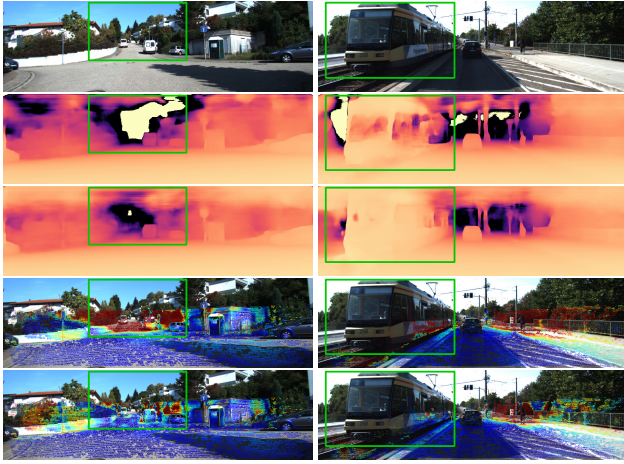


Figure 6. Row 1: Original images. Row 2: Predicted depth map without PPE. Row 3: Predicted depth map with PPE. Row 4: Error map without PPE. Row 5: Error map with PPE.

Method	Abs Rel $\downarrow$	Sq Rel $\downarrow$	RMSE $\downarrow$
baseline	0.073	0.411	3.378
+FP	0.044	0.216	2.165
+PPE	0.040	0.145	2.013
+SFB	<b>0.037</b>	0.117	1.878
+DL	<b>0.037</b>	<b>0.109</b>	<b>1.815</b>

Table 4. Ablation studies for components. The components are added incrementally. Flow pretrain is shown as FP. SFB means single frame branch. DL is the auxiliary depth loss described in Eqn. 17. PPE is proposed Planar Position Embedding.

parison between depth and  $\gamma$  shows the superiority of  $\gamma$  prediction. As in Eqn. 10,  $\gamma$  is independent of intrinsic  $\mathcal{K}$ , which improves its generalization. Above all, we conduct experiments in different pre-training, from scratch, ImageNet and optical flow. The results indicate that the model with ImageNet pre-training can not take advantage of the consecutive frame shown by the similar performance between frame one or two. On the contrary, the flow pre-training significantly improves the results. Finally, to figure out the influence of planar prior, we show the model without warping, which only uses the epipolar geometry. The results are still worse than our proposed method, which means the planar prior plays an essential role in our superior results.

**Effect of each component.** In Tab. 4, we unfold the proposed model module by module to understand how each component affects our results. We first validate the effectiveness of the essential idea, the flow pre-training. It almost halves the error. Then, Planar Position Embedding reduce the Sq Rel by more than 25%. Specifically, its influence is

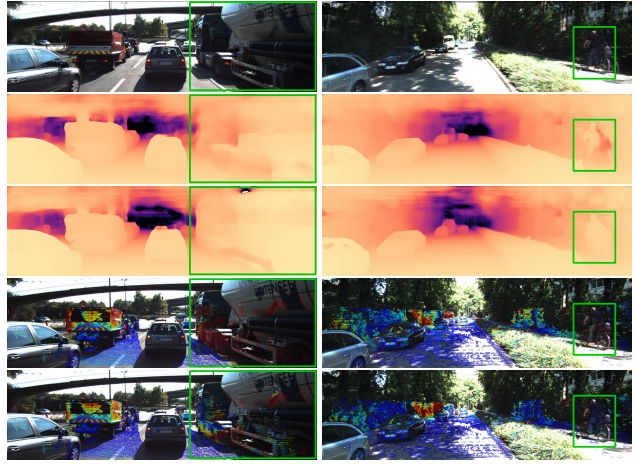


Figure 7. Row 1: Homography aligned images pairs, the first sample contains moving cars, the second sample does not have ego motion. Row 2: Predicted depth map without SFB. Row 3: Predicted depth map with SFB. Row 4: Error map without SFB. Row 5: Error map with SFB.

more intuitive in Fig. 6. Planar Position Embedding contains the pixels' position related to the ground plane, which can restrain some unreasonable errors caused by road with different slope or moving objects. As shown in Fig. 7, a single frame branch improves the performance on dynamic objects and static frames. Lastly, adding additional depth supervision makes the network learn the depth information directly, leading the error to the final level.

## 5. Conclusions and Future Work

This paper presents Planar Parallax Network, a simple but effective depth estimation framework based on planar parallax geometry. By deliberately analyzing geometric information's effectiveness, our method introduces the flow pretrain to make the network learning start from an initialization well-tuned by geometric prior. Then we handle the inherent weakness of the planar parallax pipeline by single frame estimation and Planar Position Embedding. Comprehensive experiments on KITTI and Waymo Open Dataset demonstrate PPNet surpasses the previous SOTA methods by a significant margin.

For future work, low-cost flow supervision will be a potential topic. Many unsupervised flow methods can be joint training in our framework. Furthermore, we would like to extend our method to multi-frame observation, which can provide more geometric information. Moreover, we are also interested in integrating our method into the real autonomous driving perception system.

## References

[1] Yasuhiro Aoki, Hunter Goforth, Rangaprasad Arun Srivastan, and Simon Lucey. PointNetLK: Robust & efficient point cloud registration using PointNet. In *CVPR*, 2019. 1

[2] Dietrich Baehring, Stephan Simon, Wolfgang Niehsen, and Christoph Stiller. Detection of close cut-in and overtaking vehicles for driver assistance based on planar parallax. In *IV*, 2005. 3

[3] Shariq Farooq Bhat, Ibraheem Alhashim, and Peter Wonka. AdaBins: Depth estimation using adaptive bins. In *CVPR*, 2021. 2, 5, 6

[4] Jiawang Bian, Zhichao Li, Naiyan Wang, Huangying Zhan, Chunhua Shen, Ming-Ming Cheng, and Ian Reid. Unsupervised scale-consistent depth and ego-motion learning from monocular video. *NeurIPS*, 2019. 1

[5] Jia-Wang Bian, Huangying Zhan, Naiyan Wang, Zhichao Li, Le Zhang, Chunhua Shen, Ming-Ming Cheng, and Ian Reid. Unsupervised scale-consistent depth learning from video. *IJCV*, 2021. 1

[6] Daniel J Butler, Jonas Wulff, Garrett B Stanley, and Michael J Black. A naturalistic open source movie for optical flow evaluation. In *ECCV*, 2012. 6

[7] Yang Chen and Gérard Medioni. Object modelling by registration of multiple range images. *IVC*, 1992. 5

[8] Geoffrey Cross, Andrew W Fitzgibbon, and Andrew Zisserman. Parallax geometry of smooth surfaces in multiple views. In *ICCV*, 1999. 3

[9] Nicolas Donati, Abhishek Sharma, and Maks Ovsjanikov. Deep geometric functional maps: Robust feature learning for shape correspondence. In *CVPR*, 2020. 1

[10] Alexey Dosovitskiy, Philipp Fischer, Eddy Ilg, Philip Hausser, Caner Hazirbas, Vladimir Golkov, Patrick Van Der Smagt, Daniel Cremers, and Thomas Brox. FlowNet: Learning optical flow with convolutional networks. In *ICCV*, 2015. 2, 6

[11] David Eigen, Christian Puhrsch, and Rob Fergus. Depth map prediction from a single image using a multi-scale deep network. *NeurIPS*, 2014. 2, 5, 6

[12] Huan Fu, Mingming Gong, Chaohui Wang, Kayhan Batmanghelich, and Dacheng Tao. Deep ordinal regression network for monocular depth estimation. In *CVPR*, 2018. 2, 6

[13] Andreas Geiger, Philip Lenz, and Raquel Urtasun. Are we ready for autonomous driving? the KITTI vision benchmark suite. In *CVPR*, 2012. 2, 5

[14] Clément Godard, Oisin Mac Aodha, Michael Firman, and Gabriel J Brostow. Digging into self-supervised monocular depth estimation. In *ICCV*, 2019. 2

[15] Eddy Ilg, Nikolaus Mayer, Tonmoy Saikia, Margret Keuper, Alexey Dosovitskiy, and Thomas Brox. FlowNet 2.0: Evolution of optical flow estimation with deep networks. In *CVPR*, 2017. 2

[16] Michal Irani and Prabu Anandan. Parallax geometry of pairs of points for 3D scene analysis. In *ECCV*, 1996. 2, 3

[17] Michal Irani, P Anandan, and Meir Cohen. Direct recovery of planar-parallax from multiple frames. *PAMI*, 2002. 3

[18] Joel Janai, Fatma Guney, Anurag Ranjan, Michael Black, and Andreas Geiger. Unsupervised learning of multi-frame optical flow with occlusions. In *ECCV*, 2018. 2

[19] Hualie Jiang, Laiyan Ding, Junjie Hu, and Rui Huang. PLNet: Plane and line priors for unsupervised indoor depth estimation. In *3DV*, 2021. 2

[20] Kyunghwa Jung and Jaesung Hong. Quantitative assessment method of image stitching performance based on estimation of planar parallax. *IA*, 2021. 3

[21] Johannes Kopf, Xuejian Rong, and Jia-Bin Huang. Robust consistent video depth estimation. In *CVPR*, 2021. 1

[22] Jin Han Lee, Myung-Kyu Han, Dong Wook Ko, and Il Hong Suh. From big to small: Multi-scale local planar guidance for monocular depth estimation. *arXiv*, 2019. 2, 5, 6, 7, 11, 13

[23] Seokju Lee, Sunghoon Im, Stephen Lin, and In So Kweon. Learning monocular depth in dynamic scenes via instance-aware projection consistency. In *AAAI*, 2021. 2

[24] Jiaxin Li and Gim Hee Lee. DeepI2P: Image-to-point cloud registration via deep classification. In *CVPR*, 2021. 1

[25] Qing Li, Shaoyang Chen, Cheng Wang, Xin Li, Chenglu Wen, Ming Cheng, and Jonathan Li. LO-Net: Deep real-time LiDAR odometry. In *CVPR*, 2019. 1

[26] Zhichao Li and Naiyan Wang. DMLO: Deep matching LiDAR odometry. In *IROS*, 2020. 1

[27] Ze Liu, Yutong Lin, Yue Cao, Han Hu, Yixuan Wei, Zheng Zhang, Stephen Lin, and Baining Guo. Swin Transformer: Hierarchical vision transformer using shifted windows. In *ICCV*, 2021. 2, 5

[28] Ilya Loshchilov and Frank Hutter. Decoupled weight decay regularization. *arXiv*, 2017. 6

[29] Manolis IA Lourakis and Stelios C Orphanoudakis. Using planar parallax to estimate the time-to-contact. In *CVPR*, 1999. 3

[30] Weixin Lu, Guowei Wan, Yao Zhou, Xiangyu Fu, Pengfei Yuan, and Shiyu Song. DeepVCP: An end-to-end deep neural network for point cloud registration. In *ICCV*, 2019. 1

[31] Xuan Luo, Jia-Bin Huang, Richard Szeliski, Kevin Matzen, and Johannes Kopf. Consistent video depth estimation. *ToG*, 2020. 1

[32] Reza Mahjourian, Martin Wicke, and Anelia Angelova. Unsupervised learning of depth and ego-motion from monocular video using 3D geometric constraints. In *CVPR*, 2018. 2

[33] Hanspeter A Mallot, Heinrich H Bülthoff, JJ Little, and Stefan Bohrer. Inverse perspective mapping simplifies optical flow computation and obstacle detection. *Biological cybernetics*, 1991. 5

[34] Nikolaus Mayer, Eddy Ilg, Philip Hausser, Philipp Fischer, Daniel Cremers, Alexey Dosovitskiy, and Thomas Brox. A large dataset to train convolutional networks for disparity, optical flow, and scene flow estimation. In *CVPR*, 2016. 6

[35] Simon Meister, Junhwa Hur, and Stefan Roth. UnFlow: Unsupervised learning of optical flow with a bidirectional census loss. In *AAAI*, 2018. 2

[36] Moritz Menze and Andreas Geiger. Object scene flow for autonomous vehicles. In *CVPR*, 2015. 6

[37] Adam Paszke, Sam Gross, Francisco Massa, Adam Lerer, James Bradbury, Gregory Chanan, Trevor Killeen, Zeming Lin, Natalia Gimelshein, Luca Antiga, et al. Pytorch: An imperative style, high-performance deep learning library. *NeurIPS*, 2019. 6

[38] René Ranftl, Alexey Bochkovskiy, and Vladlen Koltun. Vision transformers for dense prediction. In *ICCV*, 2021. 6

[39] Anurag Ranjan, Varun Jampani, Lukas Balles, Kihwan Kim, Deqing Sun, Jonas Wulff, and Michael J Black. Competitive collaboration: Joint unsupervised learning of depth, camera motion, optical flow and motion segmentation. In *CVPR*, 2019. 2

[40] Harpreet S Sawhney. 3D geometry from planar parallax. In *CVPR*, 1994. 1, 2

[41] Harpreet S Sawhney. Motion video analysis using planar parallax. In *Storage and Retrieval for Image and Video Databases II*, 1994. 2

[42] Harpreet S Sawhney. Simplifying motion and structure analysis using planar parallax and image warping. In *ICPR*, 1994. 3

[43] Shashua and Navab. Relative affine structure: theory and application to 3D reconstruction from perspective views. In *CVPR*, 1994. 1, 2

[44] Chang Shu, Kun Yu, Zhixiang Duan, and Kuiyuan Yang. Feature-metric loss for self-supervised learning of depth and egomotion. In *ECCV*, 2020. 2

[45] Deqing Sun, Xiaodong Yang, Ming-Yu Liu, and Jan Kautz. PWC-Net: CNNs for optical flow using pyramid, warping, and cost volume. In *CVPR*, 2018. 2

[46] Pei Sun, Henrik Kretzschmar, Xerxes Dotiwalla, Aurelien Chouard, Vijaysai Patnaik, Paul Tsui, James Guo, Yin Zhou, Yuning Chai, Benjamin Caine, et al. Scalability in perception for autonomous driving: Waymo open dataset. In *CVPR*, 2020. 2, 5

[47] Zachary Teed and Jia Deng. RAFT: Recurrent all-pairs field transforms for optical flow. In *ECCV*, 2020. 2

[48] Vaibhav Vaish, Bennett Wilburn, Neel Joshi, and Marc Levoy. Using plane+parallax for calibrating dense camera arrays. In *CVPR*, 2004. 3

[49] Chaoyang Wang, José Miguel Buenaposada, Rui Zhu, and Simon Lucey. Learning depth from monocular videos using direct methods. In *CVPR*, 2018. 2

[50] Guangming Wang, Xinrui Wu, Zhe Liu, and Hesheng Wang. PWCL-Net: Deep LiDAR odometry in 3D point clouds using hierarchical embedding mask optimization. In *CVPR*, 2021. 1

[51] Tai Wang, Jiangmiao Pang, and Dahua Lin. Monocular 3D object detection with depth from motion. In *ECCV*, 2022. 2, 4

[52] Yang Wang, Yi Yang, Zhenheng Yang, Liang Zhao, Peng Wang, and Wei Xu. Occlusion aware unsupervised learning of optical flow. In *CVPR*, 2018. 2

[53] Hao Xing, Yifan Cao, Maximilian Biber, Mingchuan Zhou, and Darius Burschka. Joint prediction of monocular depth and structure using planar and parallax geometry. *PR*, 2022. 1, 3

[54] Haofei Xu, Jing Zhang, Jianfei Cai, Hamid Rezatofighi, and Dacheng Tao. GMFlow: Learning optical flow via global matching. In *CVPR*, 2022. 2, 4, 5, 6

[55] Wei Yin, Yifan Liu, and Chunhua Shen. Virtual normal: Enforcing geometric constraints for accurate and robust depth prediction. *PAMI*, 2021. 1

[56] Wei Yin, Yifan Liu, Chunhua Shen, and Youliang Yan. Enforcing geometric constraints of virtual normal for depth prediction. In *ICCV*, 2019. 2

[57] Zhichao Yin and Jianping Shi. GeoNet: Unsupervised learning of dense depth, optical flow and camera pose. In *CVPR*, 2018. 1, 2

[58] Chang Yuan, Gerard Medioni, Jinman Kang, and Isaac Cohen. Detecting motion regions in the presence of a strong parallax from a moving camera by multiview geometric constraints. *PAMI*, 2007. 3

[59] Haobo Yuan, Teng Chen, Wei Sui, Jiafeng Xie, Lefei Zhang, Yuan Li, and Qian Zhang. Monocular road planar parallax estimation. *arXiv*, 2021. 1, 3, 5, 6

[60] Weihao Yuan, Xiaodong Gu, Zuozhuo Dai, Siyu Zhu, and Ping Tan. NeWCRFs: Neural window fully-connected CRFs for monocular depth estimation. In *CVPR*, 2022. 2, 5, 6, 7, 11, 13

[61] Huangying Zhan, Chamara Saroj Weerasekera, Jia-Wang Bian, and Ian Reid. Visual odometry revisited: What should be learnt? In *ICRA*, 2020. 1

[62] Shengyu Zhao, Yilun Sheng, Yue Dong, Eric I Chang, Yan Xu, et al. MaskFlowNet: Asymmetric feature matching with learnable occlusion mask. In *CVPR*, 2020. 2, 4

[63] Wang Zhao, Shaohui Liu, Yezhi Shu, and Yong-Jin Liu. Towards better generalization: Joint depth-pose learning without PoseNet. In *CVPR*, 2020. 1

[64] Yiran Zhong, Pan Ji, Jianyu Wang, Yuchao Dai, and Hongdong Li. Unsupervised deep epipolar flow for stationary or dynamic scenes. In *CVPR*, 2019. 2

[65] Tinghui Zhou, Matthew Brown, Noah Snavely, and David G Lowe. Unsupervised learning of depth and ego-motion from video. In *CVPR*, 2017. 1

[66] Tinghui Zhou, Matthew Brown, Noah Snavely, and David G Lowe. Unsupervised learning of depth and ego-motion from video. In *CVPR*, 2017. 2

[67] Yuliang Zou, Zelun Luo, and Jia-Bin Huang. DF-Net: Unsupervised joint learning of depth and flow using cross-task consistency. In *ECCV*, 2018. 2

## A. Planar Parallax Geometry

We provide a complete derivation process in this section. As in the main body, we use capital letter to represent 3D points, lowercase letter for 2D points, bold font for vectors, and matrix in calligraphy.

The ratio of height to depth  $\gamma$  is defined as:

$$\gamma = \frac{h}{z}, \quad (19)$$

where  $h$  and  $z$  is the height and depth of a pixel.

Define  $\mathbf{P}_s = (x', y', z')^T$  and  $\mathbf{P}_t = (x, y, z)^T$  as the coordinates of a point  $\mathbf{P}$  in source view and target view, separately. Let  $\mathcal{R}$  and  $\mathbf{T} = (t_x, t_y, t_z)^T$  denote the rotation matrix and translation vector between the two camera views. The transformation from  $\mathbf{P}_s$  to  $\mathbf{P}_t$  can be written as:

$$\mathbf{P}_t = \mathcal{R}\mathbf{P}_s + \mathbf{T}. \quad (20)$$

The height above the reference plane  $\pi$  of the point  $\mathbf{P}$  can be express as:

$$h = h_c - \vec{\mathbf{N}}^T \mathbf{P}, \quad (21)$$

where  $\vec{\mathbf{N}}^T$  is the normal of plane  $\pi$  and  $h_c$  is the height of the camera. Eqn. 21 can be transformed into:

$$\frac{h + \vec{\mathbf{N}}^T \mathbf{P}}{h_c} = 1. \quad (22)$$

By multiply  $\mathbf{T}$  by 1 in Eqn. 20, we can obtain

$$\begin{aligned} \mathbf{P}_t &= \mathcal{R}\mathbf{P}_s + \mathbf{T} \frac{h + \vec{\mathbf{N}}^T \mathbf{P}_s}{h_c} \\ &= (\mathcal{R} + \frac{\mathbf{T}\vec{\mathbf{N}}^T}{h_c})\mathbf{P}_s + \frac{h}{h_c}\mathbf{T} \end{aligned} \quad (23)$$

Let  $\mathbf{p}_s = \frac{1}{z'}\mathcal{K}\mathbf{P}_s$ ,  $\mathbf{p}_t = \frac{1}{z}\mathcal{K}\mathbf{P}_t$  and  $\mathbf{t} = \mathcal{K}\mathbf{T}$ , where  $\mathcal{K}$  is intrinsic matrix of the camera. Then we can obtain

$$z\mathcal{K}^{-1}\mathbf{p}_t = (\mathcal{R} + \frac{\mathbf{T}\vec{\mathbf{N}}^T}{h_c})z'\mathcal{K}^{-1}\mathbf{p}_s + \frac{h}{h_c}\mathbf{T} \quad (24)$$

By mutiply  $\frac{1}{z'}\mathcal{K}$  on both sides, we have:

$$\frac{z}{z'}\mathbf{p}_t = \mathcal{K}(\mathcal{R} + \frac{\mathbf{T}\vec{\mathbf{N}}^T}{h_c})\mathcal{K}^{-1}\mathbf{p}_s + \frac{h}{h_cz'}\mathbf{t}. \quad (25)$$

With the homography matrix between the two images written as:

$$\mathcal{H} = \mathcal{K}(\mathcal{R} + \frac{\mathbf{T}\vec{\mathbf{N}}^T}{h_c})\mathcal{K}^{-1}, \quad (26)$$

Eqn. 25 can be reformulated as

$$\frac{z}{z'}\mathbf{p}_t = \mathcal{H}\mathbf{p}_s + \frac{h}{h_cz'}\mathbf{t}. \quad (27)$$

By considering the z-axis of both sides, we have:

$$\frac{z}{z'} = \mathcal{H}_3\mathbf{p}_s + \frac{ht_z}{h_cz'}, \quad (28)$$

where  $\mathcal{H}_3$  denote the third row of homography matrix  $\mathcal{H}$

Note that, the z-axis of  $\mathbf{p}_s$  and  $\mathbf{p}_t$  is 1. Scaling both sides by their z-axis, we can obtain

$$\begin{aligned} \mathbf{p}_t &= \frac{\mathcal{H}\mathbf{p}_s + \frac{h}{h_cz'}\mathbf{t}}{\mathcal{H}_3\mathbf{p}_s + \frac{ht_z}{h_cz'}} \\ &= \frac{\mathcal{H}\mathbf{p}_s}{\mathcal{H}_3\mathbf{p}_s} - \frac{\mathcal{H}\mathbf{p}_s}{\mathcal{H}_3\mathbf{p}_s} + \frac{\mathcal{H}\mathbf{p}_s + \frac{h}{h_cz'}\mathbf{t}}{\mathcal{H}_3\mathbf{p}_s + \frac{ht_z}{h_cz'}} \\ &= \frac{\mathcal{H}\mathbf{p}_s}{\mathcal{H}_3\mathbf{p}_s} - \frac{\frac{ht_z}{h_cz'}}{(\mathcal{H}_3\mathbf{p}_s + \frac{ht_z}{h_cz'})} \frac{\mathcal{H}\mathbf{p}_s}{\mathcal{H}_3\mathbf{p}_s} + \frac{\frac{h}{h_cz'}\mathbf{t}}{\mathcal{H}_3\mathbf{p}_s + \frac{ht_z}{h_cz'}} \\ &= \frac{\mathcal{H}\mathbf{p}_s}{\mathcal{H}_3\mathbf{p}_s} - \frac{ht_z}{zh_c} \frac{\mathcal{H}\mathbf{p}_s}{\mathcal{H}_3\mathbf{p}_s} + \frac{h}{h_cz'}\mathbf{t}. \end{aligned} \quad (29)$$

With epipole  $\mathbf{e}_t = \frac{1}{t_z}\mathbf{t}$ ,  $\gamma = \frac{h}{z}$ ,  $\mathbf{p}_s$  warped by homography  $\mathbf{p}_w = \frac{\mathcal{H}\mathbf{p}_s}{\mathcal{H}_3\mathbf{p}_s}$ , when  $t_z = 0$ , we have

$$\mathbf{p}_t = \mathbf{p}_w + \frac{h}{h_cz'}\mathbf{t}. \quad (30)$$

When  $t_z \neq 0$ , we have

$$\mathbf{p}_t = \mathbf{p}_w - \gamma \frac{t_z}{h_c}(\mathbf{p}_w - \mathbf{e}_t). \quad (31)$$

Then we can obtain

$$\mathbf{p}_w - \mathbf{p}_t = \gamma \frac{t_z}{h_c}(\mathbf{p}_w - \mathbf{e}_t), \quad (32)$$

which can also be converted to

$$\mathbf{p}_w - \mathbf{p}_t = \gamma \frac{t_z}{h_c}(\mathbf{p}_w - \mathbf{p}_t + \mathbf{p}_t - \mathbf{e}_t) \quad (33)$$

$$(1 - \gamma \frac{t_z}{h_c})(\mathbf{p}_w - \mathbf{p}_t) = \gamma \frac{t_z}{h_c}(\mathbf{p}_t - \mathbf{e}_t) \quad (34)$$

$$\mathbf{p}_w - \mathbf{p}_t = \frac{\gamma \frac{t_z}{h_c}}{1 - \gamma \frac{t_z}{h_c}}(\mathbf{p}_t - \mathbf{e}_t) \quad (35)$$

Now we get the relationship between  $\mathbf{u}_{res} = \mathbf{p}_w - \mathbf{p}_t$  and  $\gamma$ .

## B. More Qualitative Results

In Fig. 8, we show more qualitative results of BTS [22], NeW CRFs [60] and our method. As shown in the error maps, the result have improved significantly.

In Fig. 9, we show an example of how each component affects the result. By adding flow pre-training, the performance is improved significantly on static scenes but worsened on dynamic objects that violate the static assumption

in planar parallax geometry. It suggests that, without flow pre-training, models may not take advantage of the consecutive frame. More examples are shown in Fig.10. By adding Planar Position Embedding, the unreasonable errors have been restrained. Finally, the single frame branch and depth supervision improves the performance on dynamic objects and leads the error to the final level.

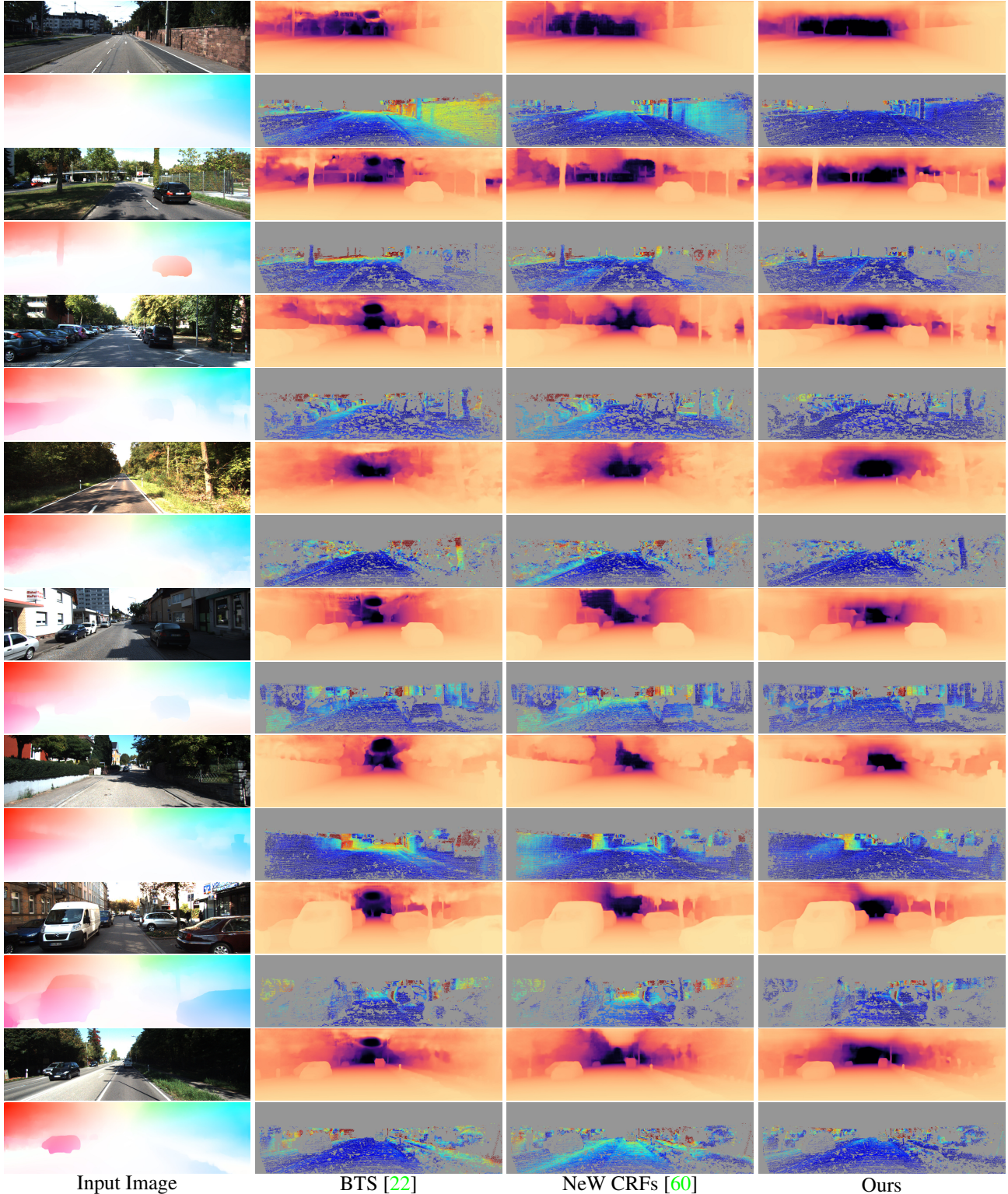


Figure 8. Qualitative results on the Eigen split of KITTI dataset. For each sample, the first column shows the target image and the flow estimated by the pre-trained optical flow model between the two plane-aligned images. The rest columns each shows the predicted depth map and the corresponding error map for a model. Blue represents smaller error, while red represents larger error.

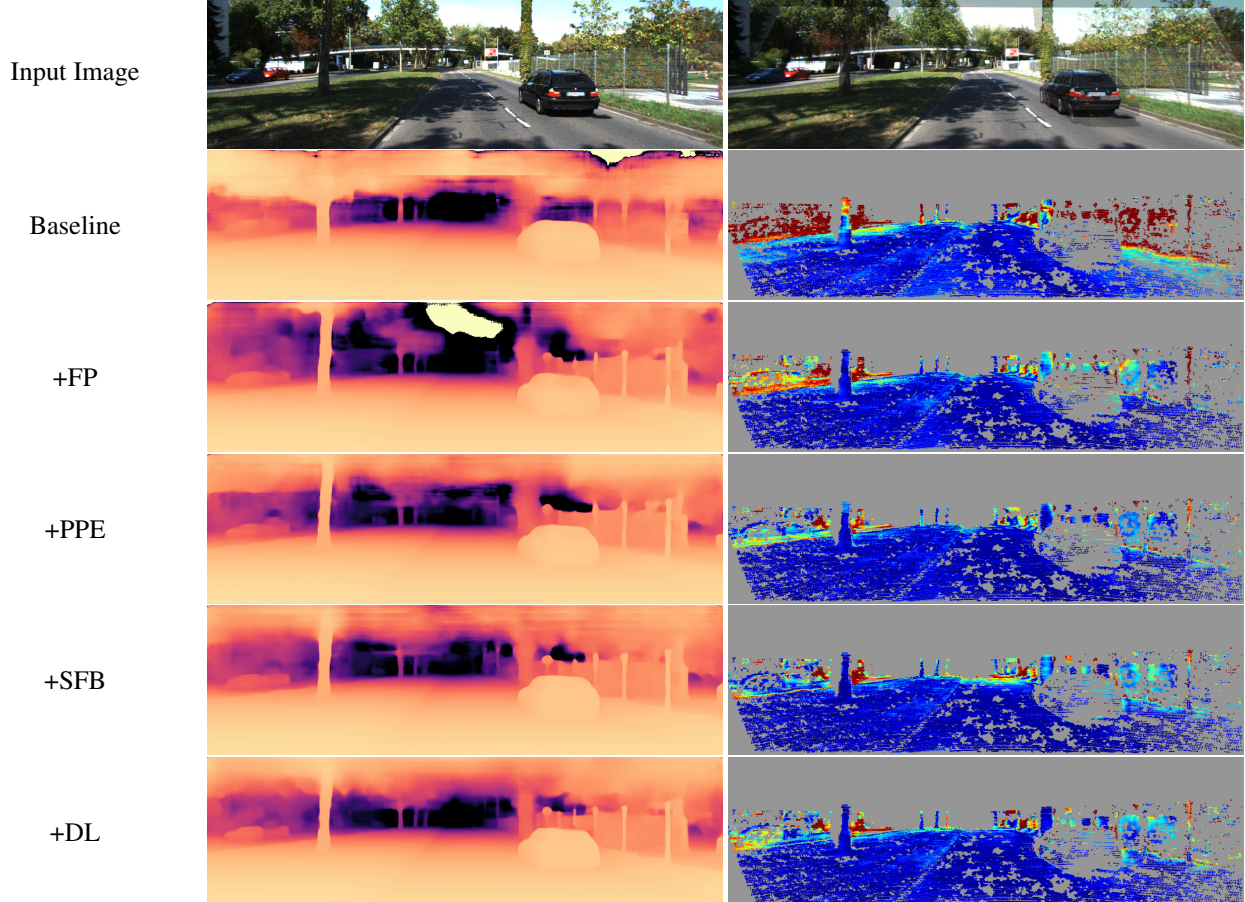


Figure 9. Qualitative results for components. The components is added incrementally. Flow pretrain is shown as FP. SFB means single frame branch. DL is the depth loss. PPE is the proposed Planar Position Embedding. The first row shows the target image and the plane-aligned image pairs. The rest rows shows the predicted depth map and the corresponding error map separately.

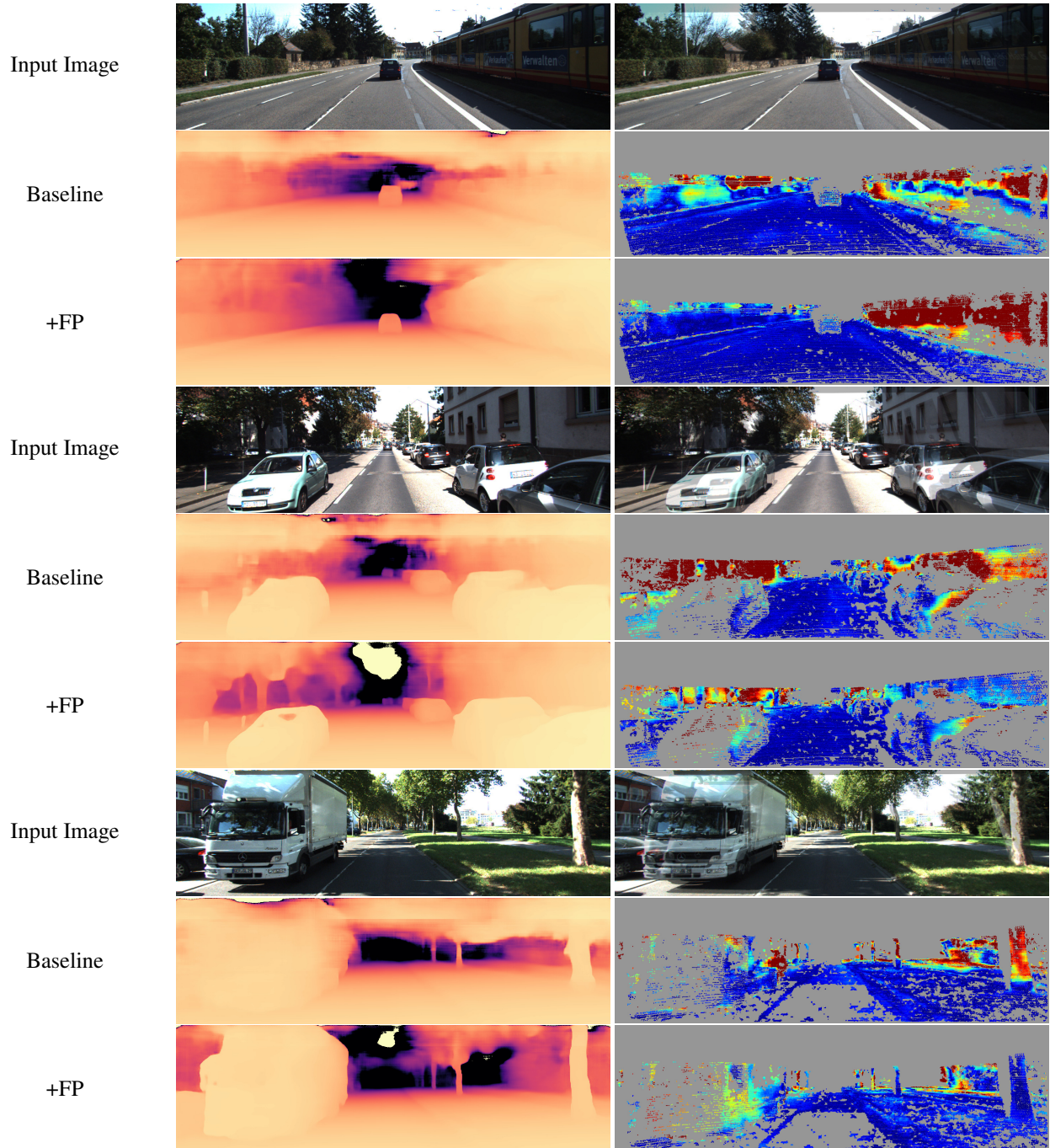


Figure 10. Comparison between baseline and +FP. For each sample, the first row shows the target image and the plane-aligned image pairs. The rest rows shows the predicted depth map and the corresponding error map separately.